Applied Materials Today 41 (2024) 102444

Contents lists available at ScienceDirect

Applied Materials Today

journal homepage: www.elsevier.com/locate/apmt

# Mechanistic understanding of enhancing bioactivity via bio-ionic liquid functionalization of biomaterials

Aihik Banerjee [a,1], Mohammad Khavani [b,1], Kevin Dalsania [a], Prince David Okoro [a], Mohammad R.K. Mofrad [b,c], Iman Noshadi [a,*]

[a] Department of Bioengineering, University of California, Riverside, Riverside, CA 92521, USA
[b] Molecular Cell Biomechanics Laboratory, Departments of Bioengineering and Mechanical Engineering, University of California, Berkeley, Berkeley, CA 94720, USA
[c] Molecular Biophysics and Integrative Bioimaging Division, Lawrence Berkeley National Lab, Berkeley, CA 94720, USA

ARTICLE INFO

*Keywords:*
Bio-ionic liquid (BIL)
Cell adhesion
Polyethylene glycol diacrylate (PEGDA)
Molecular dynamics (MD)
Digital light processing (DLP) 3D bioprinting

ABSTRACT

The selection of biomaterials is a pivotal criterion for designing tissue engineering scaffolds, crucial for diverse biomedical applications. While natural biomaterials offer inherent bioactivity and biocompatibility, fine-tuning their properties for specific applications poses challenges. Conversely, synthetic biomaterials, while highly customizable, are often bio-inert. Functionalizing materials with bioactive molecules can improve cell-material interactions. Prevailing approaches utilizing RGD peptides or natural/synthetic composites have drawbacks including cost and immunogenicity. Bio-ionic liquids (BILs), a class of biocompatible ionic liquids derived from natural or synthetic biomolecules, offer a potential alternative. Herein, we present the biofunctionalization of a bio-inert polyethylene glycol diacrylate (PEGDA) with an acrylated choline-based BIL ("BioPEG") as a method for enhancing the bioactivity of biomaterials. Cell studies using mouse myoblast C2C12 and human mesenchymal stem cells (hMSCs) revealed the excellence of BioPEG hydrogels in promoting cell attachment, growth, proliferation, and differentiation. Computational molecular dynamics (MD) simulations elucidated the mechanism by which BIL facilitates cell interaction with PEGDA. 3D printability of BioPEG hydrogel was showcased using a digital light processing (DLP) bioprinter, with printed scaffolds demonstrating excellent cytocompatibility. Collectively, these findings present BIL as a versatile bioactive agent for augmenting cell adhesion to materials, thus enriching the repertoire of biomaterials for advanced tissue engineering.

## 1. Introduction

The pressing need for novel biomaterials in the domain of cell culture scaffolding has gained significant momentum. An ideal scaffold should possess physical and chemical properties that are highly tunable to cater to diverse biomedical applications. Several promising materials have surfaced, showcasing exceptional potential for advanced tissue engineering applications, ranging from injectable cell-hydrogel constructs to 3D bioprinting [1-4]. Naturally derived materials, while often boasting excellent biocompatibility, frequently fall short as their properties are either sub-optimal or difficult to tailor for specific applications [3,5]. Specifically, natural materials often exhibit poor mechanical properties and are significantly susceptible to environmental conditions. Additionally, their propensity to provoke immunogenic reactions remains a prominent concern [6,7]. Consequently, there is a discernible shift towards the utilization of synthetic polymers, offering a remarkable degree of tunability for physical and chemical properties, coupled with minimal immunogenicity [4,8]. However, synthetic materials often exhibit limited biological activity due to the absence of proteins crucial for cell attachment [4,8].

Cell adhesion to substrates is a complex process primarily mediated by specialized molecules and structures [9,10]. When a biomaterial lacks cell adhesion-compatible surface proteins or structures, cells are unable to adhere to it, rendering the material unsuitable for cell-loading applications. The prevailing approach to address these issues involves surface functionalization of the biomaterial with appropriate proteins or molecules that enhance interaction with cell adhesion structures [10]. A commonly used method for surface functionalization of synthetic materials employs extracellular matrix (ECM) cell adhesion peptides, i.e., arginine–glycine–aspartic acid (RGD) and linkers for facilitating

---

[*] Corresponding author.
*E-mail address:* inoshadi@ucr.edu (I. Noshadi).
[1] These authors have equal contributions.

https://doi.org/10.1016/j.apmt.2024.102444
Received 2 July 2024; Received in revised form 16 August 2024; Accepted 15 September 2024

integrin-mediated cell adhesion [11,12]. A similar approach is to use other ECM proteins such as fibronectin, laminin, vitronectin, etc. to coat biomaterials in order to enhance cellular adhesion [13]. The RGD-linker or the ECM protein coating approach, while effective in enhancing biological activity, is expensive and can increase the immunogenicity of the biomaterial [14,15]. Another method to introduce desired biological properties to a synthetic material is blending with natural materials, thereby making semi-synthetic composite materials [16,17]. Although composite materials bring together the beneficial properties of their synthetic constituent with the bioactivity of the natural counterpart, issues such as inconsistent properties throughout the composite, and hence variable biological performance, the possibility of immune reaction, and the cost of production remain unsolved. Another recent method of enhancing the bioactivity of synthetic materials is the zwitterionic modification, which is described in detail elsewhere [18,19]. Certain zwitterionic-modified materials are shown to have antifouling characteristics that prevent undesirable adsorption of proteins, the first step of a foreign body rejection mechanism, while promoting cell adhesion properties [19]. Specifically, zwitterionic choline phosphates (CP), which are chemically inverse structures of phosphatidylcholine (PC), the phospholipid headgroups in all eukaryotic cell membranes, are used to modify inert materials to enhance cellular adhesion while minimizing non-specific protein binding due to the zwitterionic antifouling properties [19,20]. Although the zwitterionic strategy is promising, it suffers from critical limitations such as pH-dependent behavior, a strong hydration layer that might be conducive to bacterial growth, and fabrication challenges [21,22]. Hence, it is imperative to explore novel methods for enhancing the bioactivity of synthetic biomaterials for advanced tissue engineering and regenerative medicine applications.

In this regard, bio-ionic liquids (BILs), a class of ionic salts, characterized by positively and negatively charged groups residing on different molecules, have demonstrated the ability to confer a plethora of desirable properties to biomaterials, ranging from enhanced biocompatibility and electrical conductivity to superb antimicrobial properties, and have been thoroughly reviewed elsewhere [23,24]. Specifically, cholinium cation-based BILs have been shown to impart bioactivity to biomaterials [25,26]. Yet, their potential role in enhancing the bioactivity of bioinert materials remains largely uninvestigated. Remarkably, there is a dearth of both computational and experimental studies on the effect of BIL-modification of biomaterials on cell-biomaterial interactions. As such, it is imperative to focus on mechanistic studies of BIL-cell interaction in order to better understand the role of BILs in increasing cellular adhesion and realize its true potential as a bioactive agent.

In this study, we investigated the potential of a specific acrylated choline-based BIL in augmenting the bioactivity of a model bioinert low molecular weight polyethylene glycol diacrylate (PEGDA) hydrogel. A comparative study of cell attachment and proliferation on unmodified PEGDA and BIL-functionalized PEGDA (BioPEG) hydrogels was performed. Based on the significant enhancement of bioactivity in the functionalized hydrogels, differentiation studies were carried out on the BioPEG hydrogels to further demonstrate functional improvement. In a first-ever attempt, comprehensive computational methods were used to delineate the molecular-level mechanisms underlying BIL's role in mediating cell attachment to biomaterials. Finally, we demonstrated the advanced manufacturing of BioPEG scaffolds by 3D printing a variety of tissue engineering scaffolds, employing a digital light processing (DLP)-based optical 3D bioprinter, and analyzed the cytocompatibility of the 3D printed structures. The results underscore the tremendous potential of choline-based BILs to emerge as a new class of bioactive molecules for enhancing the biological functionality of inert biomaterials, thereby significantly increasing the arsenal of materials for use in tissue engineering and regenerative medicine applications.

## 2. Results and discussion

### 2.1. Comparative cytocompatibility of PEGDA and BioPEG hydrogels

Acrylation of choline bitartrate yielded acrylated choline-based BIL, which was conjugated to a bioinert synthetic PEGDA ($M_n$ 700) polymer to yield bioactivated BioPEG polymer (Fig. 1**A**). The detailed processes of synthesizing BIL and subsequently BioPEG hydrogels are described in the methods section. Briefly, 20 % (w/v) PEGDA and 15 % (w/v) BIL were mixed to form BioPEG, which was then crosslinked via 405 nm light-initiated photopolymerization, using lithium phenyl-2,4,6-trimethylbenzoylphosphinate (LAP) as the photo-initiator. The presence of acrylate groups in both the PEGDA polymer and the BIL facilitates easy photo-initiator-mediated photo-crosslinking to fabricate the hydrogels. We have designed our hydrogel systems to be photopolymerizable under visible light exposure since photopolymerization offers several benefits such as precise spatiotemporal control over polymerization, a non-contact process, independence from pH and temperature variations, and, most importantly, low cytotoxicity [27]. These features can be especially advantageous for biomedical applications where cell viability and gentle processing conditions are crucial. Extensive chemical characterization of BioPEG synthesized using the described method has been reported elsewhere [25].

Biomaterials intended for use as cell culture scaffolds need to be stable under standard cell culture conditions, necessitating material characterization. As such, degradation rate and swelling ratio studies were performed on the BioPEG hydrogels in 1X phosphate-buffered saline (PBS) under standard cell culture conditions of 37 °C, with 1X PBS exchanges every 2–3 days. The degradation studies (**Fig. S1A**) conducted on the BioPEG, revealed only about 5.5 % weight loss after 4 weeks, while the swelling studies (**Fig. S1B**) showed a maximum swelling ratio of 3 after 2 h in 1X PBS, which confirmed the stability of the BioPEG hydrogels for use as a scaffold for cell culture. Additionally, when the BioPEG hydrogels were subjected to compressive forces, a typical compressive stress-strain profile was obtained (**Fig. S1C**). The compressive modulus of the BioPEG hydrogels was calculated to be about 72 ± 22 kPa. The mechanical testing of cell culture biomaterials is paramount to determine the substrate stiffness, which has an important bearing on the observed cell behavior. Different cells can respond differently to similar substrate stiffness, which is a governing factor in the design of biomaterials [28]. Although all cell experiments in this study were done on hydrogels with an average stiffness of about 72 kPa, the stiffness can be easily adjusted by changing the hydrogel composition or photo-crosslinking light parameters such as intensity and duration to meet different requirements. Interestingly, hydrogels with similar stiffness values have been reported to enhance osteogenic differentiation of hMSCs [29].

Mammalian cells were cultured on both PEGDA and BioPEG hydrogels to assess cytocompatibility, utilizing a commercial live/dead cell viability assay. Human mesenchymal stem cells (hMSCs) were utilized for seeding onto these hydrogels to monitor their viability, growth, and proliferation over 14 days. Fluorescent images capturing live/dead staining were acquired on days 1, 7, and 14 post-seeding, with viable cells represented in green and dead cells in red (Fig. 1B). Remarkably, BioPEG hydrogels demonstrated superior cytocompatibility, exhibiting a significant increase in viable cells, with nearly 99 % viability seen on all assay time points, while the presence of dead cells was negligible. Conversely, PEGDA hydrogels showed a distinct lack of cell adhesion and viability, as evidenced by the significantly lower presence of live cells and more dead cells on their surface (Fig. 1B, D). While the findings suggest enhanced cytocompatibility of BioPEG hydrogels compared to PEGDA hydrogels, it is imperative to acknowledge the inherent limitation of live/dead cell assays in providing comprehensive insights into cellular vitality. Although such assays offer binary distinctions between viable and non-viable cells, they offer only a restricted view of broader cellular health parameters. Cell growth and proliferation, pivotal

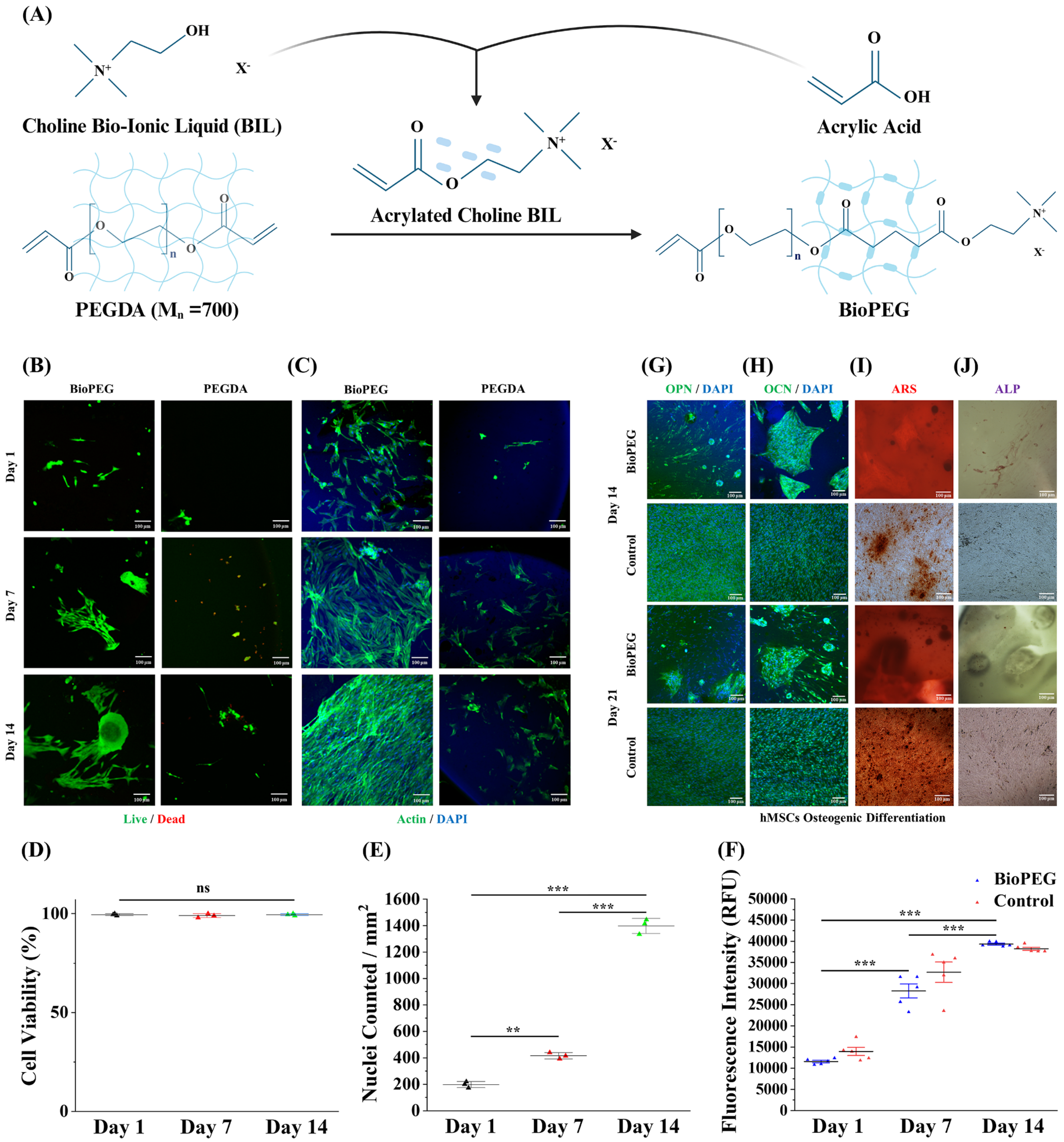

**Fig. 1. Synthesis of BIL and BioPEG.** (A) Schematic representation of the formation of the acrylated choline bio-ionic liquid (BIL) and its subsequent conjugation with polyethylene glycol diacrylate (PEGDA) to yield BioPEG. **Impact of BIL functionalization on the bioactivity of PEGDA hydrogels.** Fluorescence imaging analysis of human mesenchymal stem cells (hMSCs) cultured on BioPEG hydrogels demonstrated enhanced cell attachment and proliferation in comparison to PEGDA hydrogels lacking BIL functionalization. (B) The viability of hMSCs is depicted through live and dead staining, utilizing calcein-AM (green) and ethidium homodimer-1 (red), respectively. (C) Visualization of F-actin (green) and nuclei (blue), stained with phalloidin and 4′,6-diamidino-2-phenylindole (DAPI), respectively, providing insights into cellular morphology **(scale bar: 100 µm)**. Quantitative assessment of hMSCs on BioPEG hydrogels included (D) cell viability derived from live and dead cell assay images, (E) cell proliferation assessed through counting DAPI-stained cell nuclei, and (F) fluorescence intensity measured via PrestoBlue assay on days 1, 7, and 14 after cell seeding. Data represent means ± SD in (D) and (E), means ± SEM in (F), and statistical significance was determined by one-way ANOVA with Tukey's post hoc test ($n = 3$ in (D) and (E), $n = 5$ in (F), $*p < 0.05$, $**p < 0.01$, $***p < 0.001$, ns – non-significant). **Assessment of osteogenic differentiation of hMSCs on BioPEG hydrogels. (G, H)** Immunofluorescence staining of hMSCs cultured on BioPEG hydrogels and tissue culture plates (control) for 14 and 21 days using osteogenic differentiation induction medium revealing extensive osteogenic differentiation, as evidenced by the expression of (G) osteopontin (OPN) and (H) osteocalcin (OCN), with nuclei counterstained by DAPI. **(I, J)** Cytochemical analysis elucidating osteogenic differentiation through the detection of calcium deposition and alkaline phosphatase activity using (I) alizarin red S (ARS) and (J) alkaline phosphatase (ALP) stains, respectively **(scale bar: 100 µm)**.

indicators of positive cellular interaction with biomaterials, were further evaluated through phalloidin and 4′,6-diamidino-2-phenylindole (DAPI) staining for actin filaments and nuclei, respectively. Actin cytoskeletal spreading, indicative of cell growth and morphology, along with the gradual increase in DAPI-stained nuclei, reflecting proliferation, were examined using fluorescence microscopy on days 1, 7, and 14. Consistent with the viability assays, BioPEG hydrogels demonstrated a notable increase in both the number of cell nuclei (depicted in blue) and typical F-actin spread (depicted in green), while PEGDA samples exhibited limited phalloidin/DAPI staining with poor cellular morphology

(Fig. 1C). Cell proliferation on the BioPEG hydrogels was quantified by counting DAPI-tagged cell nuclei per unit area, as depicted in Fig. 1E. Both cellular adhesion to biomaterials and the biomaterial's capacity to sustain a supportive cellular microenvironment are pivotal factors in determining the efficacy of biomaterials. It is noteworthy that while cells may initially adhere to a material, their eventual detachment and demise could occur if the material fails to sustain optimal conditions for cellular functionality. Hence, mere cellular adhesion to a material cannot solely substantiate its cytocompatibility. In order to gain further insights into the metabolism of hMSCs on and around BioPEG hydrogels, the PrestoBlue cell viability assay was conducted on days 1, 7, and 14. The fluorescence readout revealed a progressive increase in the number of metabolically intact cells over the culture period (Fig. 1F). Notably, both positive controls and BioPEG samples displayed a significant increase in metabolically active cells throughout the culture duration, underscoring the remarkable cytocompatibility of BioPEG hydrogels. Furthermore, cytocompatibility assessments conducted on PEGDA and BioPEG hydrogels using immortal mouse myoblast C2C12 cells exhibited analogous trends, with BioPEG hydrogels outperforming PEGDA hydrogels, as illustrated in **Fig. S2**.

Cell adhesion to biomaterials is a key first step dictating a series of vital cell functionalities such as growth, proliferation, and ultimately differentiation. Our results indicated that BioPEG hydrogels significantly enhance the initial attachment of cells, leading to successful cell growth and proliferation to the extent necessary for cell-density-dependent functions such as differentiation. Although there are a number of studies showcasing different methods of enhancing cell adhesion and/or cell activity on biomaterials [30–32], our data showed that BIL functionalization is a simple and inexpensive method with excellent cytocompatibility outcomes. Due to the aforementioned advantageous properties of BILs, including high biocompatibility and low immunogenicity, BIL-modified biomaterials could be more promising for a wide range of tissue engineering and biomedical applications.

### *2.2. Osteogenic differentiation of hMSCs on BioPEG hydrogels*

As hMSCs demonstrated robust growth on BioPEG hydrogels, an investigation into the osteoconductive potential of the hydrogel was conducted utilizing a medium comprising dexamethasone, β-glycerophosphate, and ascorbic acid for osteogenic differentiation induction. Following a five-day pre-culture in regular hMSC maintenance medium to achieve confluency on the hydrogels, hMSCs were subjected to osteogenic differentiation induction medium for periods of 14 and 21 days. Given the multi-stage nature of hMSC differentiation into osteoblasts, osteoclasts, and osteocytes, involving the expression of osteoprogenitor-specific markers and matrix mineralization, we employed not only conventional alizarin red S (ARS) and alkaline phosphatase (ALP) staining assays but also immunofluorescent staining to monitor stage-specific biomarker expression throughout the differentiation process. Fig. 1 illustrates the assessment of hMSC osteogenic differentiation on BioPEG hydrogels, utilizing immunostaining for osteopontin (OPN) and osteocalcin (OCN) proteins, followed by confocal laser scanning microscopy (Fig. 1**F and G**), along with staining for calcium mineral deposits (ARS) and ALP activity, visualized through brightfield color microscopy (Fig. 1**H and I**) at 14 and 21 days post-osteogenic induction. OPN plays a pivotal role in bone remodeling processes, including osteoclastogenesis and bone matrix modulation, while OCN, a bone-specific protein primarily expressed during late osteogenesis, serves as a key biomarker for assessing osteogenic differentiation. Immunofluorescence analysis on both day 14 and day 21 revealed robust signal intensity, confirming hMSC differentiation into osteoblasts and osteoclasts (Fig. 1**F and G**). The consistent staining for ARS and ALP at both time points further corroborated the successful osteogenic differentiation of hMSCs into mature osteocytes (Fig. 1**H and I**).

Similar positive differentiation outcomes were observed in *in vitro* myogenic differentiation studies conducted with immortal mouse myoblast C2C12 cells on BioPEG hydrogels, showing positive immunofluorescence staining for myogenic differentiation markers – myogenin and myosin heavy chain-I (MHC-I) (**Fig. S2**). These findings underscore the remarkable potential of BioPEG-based biomaterials as biocompatible platforms for cell culture applications. Notably, the enhanced biocompatibility of BioPEG can be attributed to the BIL biofunctionalization, thus imparting bioactivity to an otherwise inert PEGDA.

The interesting finding from the cytocompatibility studies that BIL transforms an otherwise bio-inert PEGDA into a highly bioactive hydrogel prompted us to investigate the mechanism by which BIL enhances cell-biomaterial interactions. We hypothesize that the increase in cellular adhesion on BioPEG hydrogels is due to an ionic interaction between the choline and bitartrate groups on the hydrogel and the phosphatidylcholine head group of the lipid bilayer in the cell membrane. Currently, experimental techniques to study cellular adhesion to biomaterials are complex and often only indirectly quantify adhesion by the force exerted by a single cell or cells on the biomaterials [9,33-34]. Investigating and quantifying the interaction between a chemical group on a biomaterial and the cell membrane can be particularly challenging and imprecise, especially under physiological/live conditions. In this regard, appropriately designed computational modeling studies can generate large amounts of data providing enormous insight into complex physicochemical processes that are otherwise difficult to obtain empirically. As such, we studied the BIL-cell membrane interactions by computationally modeling the system at the molecular level.

### *2.3. Computational insights into BIL-mediated cell-biomaterial interactions*

Considering the structural properties and thickness of the lipid membranes, it is difficult to investigate and characterize the interface structure between BIL and the lipid bilayer using experimental methods. Therefore, it is of interest to analyze how BIL interacts with the biological membrane to elucidate the mechanism of the complexation process at the molecular level. In this context, molecular dynamics (MD) simulations were applied to study the possible interactions between BIL and the 1,2-dipalmitoyl-sn-glycero-3-phosphocholine (DPPC) lipid bilayer as well as the role of the BIL on the structural features and stability of the lipid membranes.

The proposed chemical structures of the cation and its counterion (bitartrate) of the BIL are presented in Fig. 2**A**. As can be seen from this figure each branch of the cation part has three $NMe_3^+$ groups, therefore, each cation of the BIL has 9 positive charges. The different chemical or molecular structures considered in the computational simulations are presented in **Fig. S3-6**. Since the designed BIL can be considered a bio-adhesive or an adhesive between two biological membranes, its interactions with the membrane were investigated by placing it between two lipid bilayers (**Fig. S6**). The details of the multistep MD simulations to assess BIL-cell membrane interactions are provided in the methods section. As can be seen from Fig. 2**B and C**, cholesterol (CHL) inside the composition of the lipid membrane changes the features of the BIL complexes with the bilayers. CHL can be effective on the fluidity of the bilayer, which by reducing the fluidity of the membrane decreases the interactions between BIL and lipid units. The obtained structures after simulation time indicated that BIL could decrease the distance between two DPPC lipid membranes. This means that BIL can increase the interactions between biological membranes and can be considered a bio-adhesive. In contrast to pure DPPC, the BIL does not show considerable interactions with the bilayer including CHL units (Fig. 2**C**), confirming that CHL decreases the affinity of the BIL towards the membrane. Area per lipid and membrane thickness are important features that can be employed to indicate structural changes and stability of the membrane in the presence of the BIL. The obtained results indicate that CHL reduces the area per lipid values from 49.97 to 39.35 $Å^2$, meaning that CHL units decrease the dynamicity of the membrane by elevating the stiffness of the system (Fig. 2**D**). Moreover, the computed

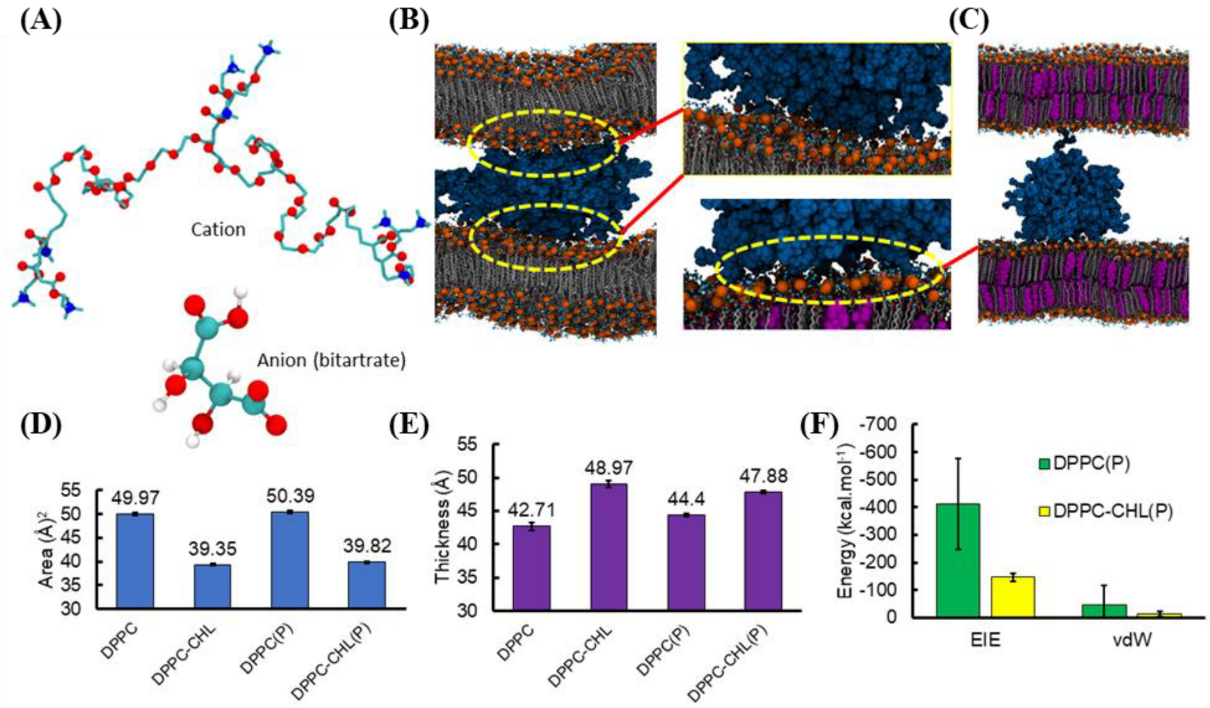

**Fig. 2.** The proposed chemical structure of the synthesized bio-ionic liquid (BIL) with choline as the cation and bitartrate as the anion (A), in which each cation has nine $NMe_3^+$ groups. The final structures of the double-layer 1,2-dipalmitoyl-sn-glycero-3-phosphocholine (DPPC) in the absence (B) and presence (C) of cholesterol (CHL) in complexation with BIL. For clarity, ions, water, and anion molecules are not presented in panels (B) and (C). In panels, (B) and (C), DPPC, cholesterol, and polymer structures are presented in gray, purple, and dark blue colors, respectively. The calculated average values of area per lipid (D) and thickness (E) of the lipid membranes in the presence and absence of the BIL and the calculated average electrostatic (EIE) and van der Waals (vdW) interactions between the BIL and different lipid bilayers (F). The (P) in DPPC(P) or DPPC-CHL(P) in the corresponding panels shows the calculated results in the presence of the BIL.

area per lipid values in the presence and absence of the BIL do not show significant differences for both lipid membranes (with/without CHL) because the BIL lies on the membrane surface and does not penetrate (Fig. 2**B and C**).

The dynamicity of the lipid membrane can be investigated by evaluating the membrane thickness during the simulation time. The membrane thickness is the distance between two phosphorus atoms of the lipid units in opposite leaflets considering the middle point between them. The membrane including CHL units shows greater membrane thickness compared with the pure DPPC bilayer (Fig. 2**E**). The significant elevation in membrane thickness in the presence of CHL groups represents that cholesterol decreases the dynamicity of the biological membranes. On the other hand, the calculated corresponding values in the presence of the BIL indicate that the complexation process decreases the dynamicity of the DPPC membrane. The computed thickness value for the DPPC in the absence of the BIL is 42.71 Å, which increases up to 44.40 Å in the complexation form. This result reveals that BIL lies on the surface of the lipid membranes and could increase the stability of the bilayers. Based on the obtained results BIL has more interaction with the DPPC lipid bilayer by increasing the membrane thickness by about 1.69 Å compared with the DPPC—CHL membrane. Cholesterol by decreasing the charge of the membrane surface reduces the possible interactions between BIL and membrane surface, therefore BIL is less effective on the features of the lipid bilayer (area per lipid and thickness) in the presence of CHL. To analyze the affinity of the BIL towards lipid membranes the number of contacts (cutoff 5 Å) between BIL and head groups was calculated. As can be seen from **Fig. S7**, the calculated number of contacts decreased by about 70 % in the presence of the CHL groups. This result indicates that the affinity of the BIL and its effects on the biological systems not only depend on the features of the BIL but also are related to the membrane composition. Therefore, it is possible to tune the properties and affinity of the designed BIL based on the composition of the host tissue. The complexation process between BIL and membrane surface occurs through a combination of electrostatic (EIE) and van der Waals (vdW) interactions. Both interaction energies decreased in the presence of CHL units. As can be seen from Fig. 2**F**, the CHL reduces the electrostatic and vdW interactions between BIL and lipid membrane by about 362 and 133 kcal.mol$^{-1}$, respectively. The computed interaction energies between DPPC and BIL show that the designed biopolymer has considerable affinity towards the biological membrane and can form stable complexes with the DPPC membrane, in agreement with the experimental observation. One reason for this considerable interaction could be an attractive force between $PO_4^-$ groups of the membrane and positively charged branches of the BIL. The structural analysis indicates that $PO_4^-$ groups of the lipid membrane can form salt bridge interactions (strong electrostatic interaction) with $NMe_3^+$ groups of the BIL (cation part). On the other hand, there is another important interaction between $COO^-$ groups of the cation and $NMe_3^+$ of the lipid units. The strength of the calculated electrostatic and vdW interactions indicates that electrostatic interaction can be considered the driving force for the complexation process, which is promoted by salt bridge formation between $PO_4^-$ and $NMe_3^+$ groups.

Radial distribution function (RDF) analysis was applied to investigate the distribution of $COO^-$ and $NMe_3^+$ groups of the BIL around the head part of the membrane. As can be seen from Fig. 3**A**, the calculated intensity for the $PO_4^-$-$NMe_3^+$ is more than the obtained corresponding value for the $COO^-$—$NMe_3^+$ interaction. It means that $NMe_3^+$ groups of the BIL have stronger interactions with the $PO_4^-$ groups of the lipid units compared with the $COO^-$ interactions with the $NMe_3^+$ groups. Moreover, the greater intensity of the corresponding interactions confirms that this interaction ($PO_4^-$-$NMe_3^+$) has more contribution in the complexation process between BIL and lipid membrane (Fig. 3**B**). On the other hand, the calculated RDFs show a sharp peak at the distance of 3.25 Å, meaning that the $COO^-$ and $NMe_3^+$ groups of the BIL lie at this distance

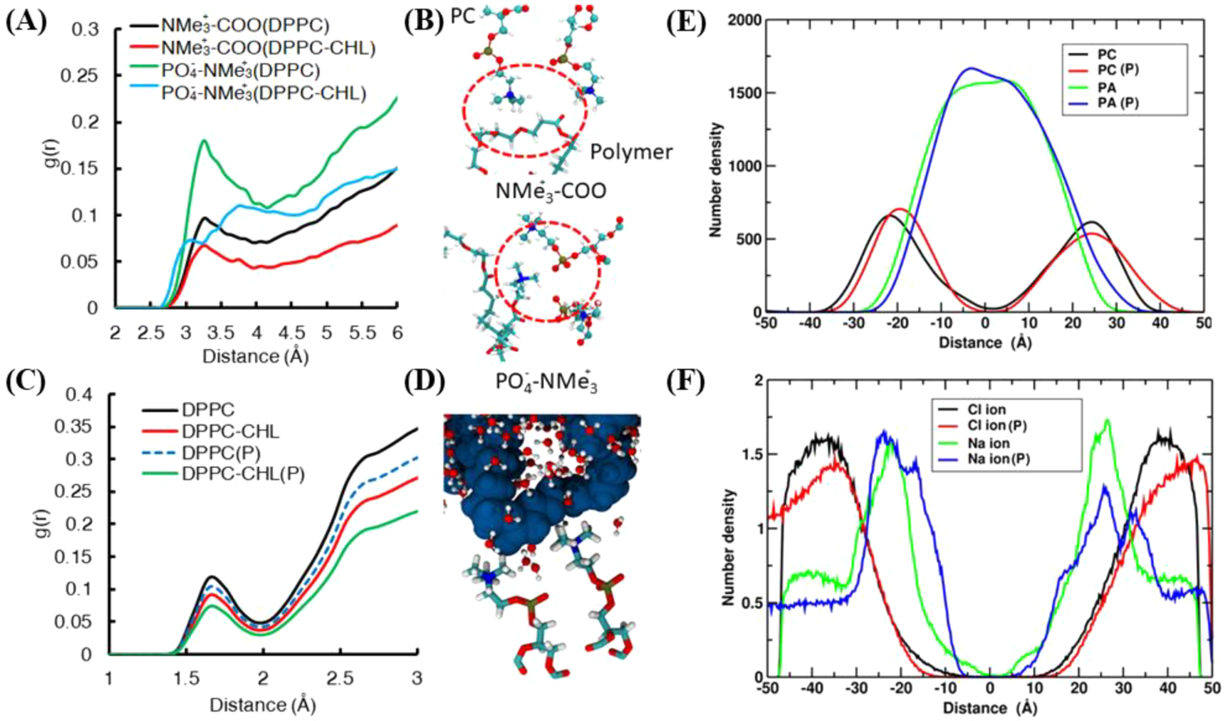

**Fig. 3.** The calculated radial distribution function, g(r), between the functional groups of the bio-ionic liquid (BIL) ($COO^-$ and $NMe_3^+$) and $NMe_3^+$ and $PO_4^-$ groups of the lipid membranes (A) and the schematic presentation of the interactions between corresponding functional groups (B). The calculated g(r) between water molecules and head groups of the lipid membranes in the presence and absence of the BIL (C) and the schematic presentation of the water orientations around the head groups in the presence of the BIL (D). The calculated number density profiles of the DPPC in the absence and complexation with BIL (E) and the number density profiles for the ion distribution on the surface of the DPPC in the presence and absence of the BIL (F).

relative to the head groups (DPPC). The comparison between the calculated RDFs in the presence and absence of CHL groups indicates that BIL has more affinity towards the pure membrane than the DPPC—CHL system, in agreement with previous results. BIL, by changing the solvation shell and charge distribution around the membrane surface, is effective in the stability and dynamical behavior of the lipid bilayer. According to the obtained RDF for water distribution around the head groups, BIL competes with water molecules to interact with the head groups (Fig. 3**C**). In other words, BIL changes water distribution on the membrane surface, which plays a key role in the stability of the lipid bilayers. As can be seen from Fig. 3C, the calculated RDFs show that water molecules lie at a distance of 1.70 Å relative to the membrane surface, which confirms H-bond formation between water molecules and head groups (Fig. 3**D**).

The density distribution profile (Fig. 3**E**) represents that BIL is in more interaction with the head group of the lipid membrane than the tail part because BIL lies on the membrane surface and does not show any penetration. Moreover, the ion distribution in the presence and absence of the BIL indicates that $Na^+$ ions lie at a closer distance relative to the membrane surface compared with $Cl^-$ ions (Fig. 3**F**) due to the nature of the membrane surface. BIL through changing charge distribution on the membrane surface influences the stability of the lipid membranes. According to the obtained charge density profiles for the lipid membranes (**Fig. S8**), CHL groups reduce the effects of the BIL on the charge perturbation of the membrane. The charge density profile shows more reduction around the head groups (PC unit) of the membranes compared with the tail part (PA unit), confirming strong interactions between charged groups of the BIL and membrane surface. The BIL is not only effective on the charge distribution of the membrane surface but also influences the charge distribution around water molecules and the entire charge distribution in the system (**Fig. S8**). This observation clearly confirmed that BIL has considerable affinity towards the lipid bilayer that, due to strong interactions with the surface, changes water distribution on the membrane surface as well as the structural features of the bilayer. Overall, MD simulations indicated that BIL can form stable complexes with the DPPC membrane, and the adsorption process occurs through electrostatic and vdW interactions, in which the electrostatic interactions are promoted by salt bridge formation between positively charged branches of the BIL and $PO_4^-$ groups of the membrane. Although the use of computational simulations for gaining atomistic understanding of cell adhesion mechanisms has been published [35-37], the use of MD simulations to understand the mechanisms by which BIL mediates cell-biomaterial interactions has not been reported previously.

Having established a mechanism of action of BILs in mediating cell-biomaterial interaction, a suitable advanced method of fabrication of cell culture scaffolds using BioPEG hydrogels was investigated. Development of advanced manufacturing of biomaterials will pave the way for optimal production and faster incorporation of innovative biomaterials in a diverse array of industries, ranging from bio-electronics and biosensors to the pharmaceutical and healthcare industries. In this regard, additive manufacturing or 3D printing, one of the most promising advanced manufacturing techniques, was explored using BioPEG hydrogel solution as the bio-ink.

### *2.4. Digital light processing (DLP) 3D printing with BioPEG bio-ink*

3D bioprinting, a subset of additive manufacturing, facilitates the fabrication of biocompatible 3D scaffolds, enabling extensive control over configurations of either cell-laden (3D encapsulation) or cell-covered (2D surface) constructs. These scaffolds hold immense promise across diverse domains, particularly in organ-on-a-chip systems for disease modeling and tissue engineering endeavors [38]. Primarily, 3D bioprinting techniques fall into two categories: extrusion and optical printing. Extrusion printing operates on the principle of a mobile printhead depositing material along a predetermined trajectory to form complete layers [39]. Layer upon layer, the scaffold gradually forms, offering relatively economical fabrication albeit with inherent challenges such as precise control over bio-ink viscosity, prolonged print durations for larger constructs, heightened shear stress on cells during printing, limited resolution compared to alternative methods, and susceptibility to nozzle clogging. Given these limitations, attention has shifted towards optical bioprinting methods, which encompass technologies such as stereolithography (SLA) and digital light processing (DLP). Among these, DLP emerges as a favored option for scaffold fabrication due to its simplicity and rapidity. In DLP printing, a photopolymerizable bio-ink undergoes curing upon exposure to ultraviolet (UV) or visible light, typically at a wavelength of 405 nm. A computer-assisted design (CAD) model is sliced into X-Y layers, each assigned a specific thickness, and as the printing progresses, the scaffold is incrementally built up by curing successive layers of bio-ink. Notably, the entire layer is cured at once, resulting in expedited printing and nozzle-less printing minimizes shear stress on cells [40]. Capitalizing on these advantages, we have opted to develop a bio-ink, based on the BioPEG hydrogel, and utilize DLP 3D printing technology with the Cellink Lumen-X Gen 1 3D bioprinter.

Employing the BioPEG hydrogel as a bio-ink, with a composition identical to the BioPEG hydrogel solutions utilized for cytocompatibility testing, the DLP 3D printer was utilized for fabricating 3D printed constructs. The BioPEG bio-ink comprised PEGDA, the cellular adhesion agent BIL, the photo-initiator LAP, and additionally a photo-absorber tartrazine. The photo-absorber serves a crucial role in moderating the extent of crosslinking and governing polymerization within unmasked regions. However, excessive addition of the photo-absorber may lead to undesirable outcomes such as under-crosslinking, prolonged layer cure times, or incomplete prints, as observed in our experiments and corroborated by prior literature [41]. Tartrazine was selected as the photo-absorber due to its efficacy in maintaining high-resolution printing capabilities, albeit with potential cytotoxic or mutagenic implications [42]. Consequently, the bio-ink formulation was optimized to minimize tartrazine concentration while preserving high-resolution printability.

The optimization process for achieving the desired scaffold resolution encompassed a three-step approach: initial determination of the minimum tartrazine concentration required for printability, identification of optimal print settings for simple structures through comparison of the printed structures with their respective CAD models, and iterative refinement of print parameters for increasingly complex structures until optimal resolution was attained. The minimum tartrazine concentration was established utilizing a card CAD model, wherein power and layer time settings were systematically adjusted within the range of 50 % to 80 % power and 4 to 8 s layer time. Subsequent optimization steps relied on a variety of CAD models to iteratively adjust printer settings, gradually refining resolution until satisfactory outcomes were achieved. During each iteration, the printed scaffolds underwent meticulous examination against the respective CAD models to discern indications of over-polymerization or under-polymerization, guiding the selection of the optimal tartrazine concentration and print settings. Preliminary experimentation identified a tartrazine concentration of 0.02 % (w/v) with print settings of 50 % power and 8 s layer time as optimal. Following the verification with a high-resolution heart structure printing, models were reprinted utilizing optimized settings, incorporating a layer height of 50 μm, 50 % power (15.66 mW/cm$^2$), 6.25 s layer time, and 1X burn-in. The printability of the optimized BioPEG bio-ink using the DLP 3D printer was demonstrated by printing structures of varying complexity, from a simple lattice to a complex heart structure as depicted in Fig. 4**A**.

3D printed BioPEG samples intended for cytocompatibility assessment underwent post-printing tartrazine leaching and thorough sterilization processes. Cell studies using hMSCs conducted over a span of 14 days revealed the cytocompatibility of the 3D printed structures, with nearly 100 % viability observed at both day 7 and day 14-time points, as determined by the calcein AM/ethidium homodimer-1-based live/dead cell viability assay (Fig. 4**B, D**). Additionally, the proliferation and spreading of hMSCs on the printed constructs, assessed through phalloidin/DAPI-based staining of F-actin cytoskeleton and nuclei, respectively, were comparable to positive controls by the day 14-time point (Fig. 4**C, E**). Thus, the BioPEG bio-ink, in tandem with the DLP printer, achieves exceptional resolution, faithfully preserving intricate details from CAD models, while demonstrating high cytocompatibility.

## 3. Conclusion

BioPEG demonstrates remarkable advantages in terms of cell attachment and proliferation when compared to PEGDA hydrogels. The ability of BioPEG to support the differentiation of hMSCs into osteoblasts, osteoclasts, or osteocytes, and C2C12 cells into myofibers underscores its efficacy, facilitated by the attainment of cell confluency necessary for initiating differentiation protocols. Our investigation delved into the intricate mechanisms underlying BIL-mediated enhancement of cell-biomaterial interactions through extensive computational simulation analyses. Notably, our findings illuminate the transformative potential of BIL, which converts neutral biomaterials into highly interactive substrates. The surface modifications upon BIL functionalization of compatible biomaterial involve the integration of chemical structures capable of engaging with lipid bilayer components in cell membranes, thereby promoting cell adhesion to the material through electrostatic and vdW interactions. Furthermore, the advanced manufacturing of BioPEG scaffolds was substantiated through DLP-based 3D printing applications using BioPEG hydrogel solution as the bio-ink, with subsequent cell studies on the printed constructs revealing exceptional cell viability and proliferation. In summation, this study not only offers an innovative alternative to natural peptides for enhancing cell-biomaterial interactions but also provides a comprehensive examination of the mechanistic underpinnings of the role of BIL in enhancing the bioactivity of bio-inert substrates.

## 4. Methods

The majority of the chemicals utilized in this study were obtained from Sigma-Aldrich (St. Louis, MO, USA) unless explicitly specified. Analytical reagent-grade chemicals were employed without further purification.

### *4.1. Synthesis of PEGDA and BioPEG hydrogel solutions*

First, acrylated choline BIL was synthesized by reacting choline bitartrate (80 % (w/v) in distilled water) with acrylic acid at a 1:1 molar ratio at 50 °C for 5 h under an inert nitrogen environment [25,26]. The acrylated choline BIL was washed extensively with ethyl acetate to remove unreacted acrylic acid. Any traces of ethyl acetate were removed during further purification of the synthesized BIL by rotary vacuum evaporation overnight at 60 °C. The purified BIL was frozen at −80 °C for 24 h and then freeze-dried for 2 days. To form the BioPEG hydrogel solution, PEGDA ($M_n = 700$, Sigma Aldrich) and BIL were added to 1X PBS at final concentrations of 20 % (w/v) and 15 % (w/v), respectively, and mixed with the photo-initiator LAP at 0.2 % (w/v). The resulting BioPEG hydrogel solution was pH adjusted to 7 using 10 M NaOH. The PEGDA hydrogel solution was made by mixing 20 % (w/v) PEGDA with 0.2 % (w/v) LAP in 1X PBS. A 405 nm visible light source (20 mW/cm$^2$) attached to an Allevi 2 bioprinter was used to photo-crosslink the hydrogel solutions for 60 s.

### *4.2. Sample preparation for degradation, swelling, and mechanical characterization of BioPEG hydrogels*

Cuboid-shaped samples of the BioPEG hydrogels were DLP 3D printed via the use of a simple solid cuboid CAD file with the dimensions 11 mm by 11 mm by 3 mm (length x breadth x height) designed in

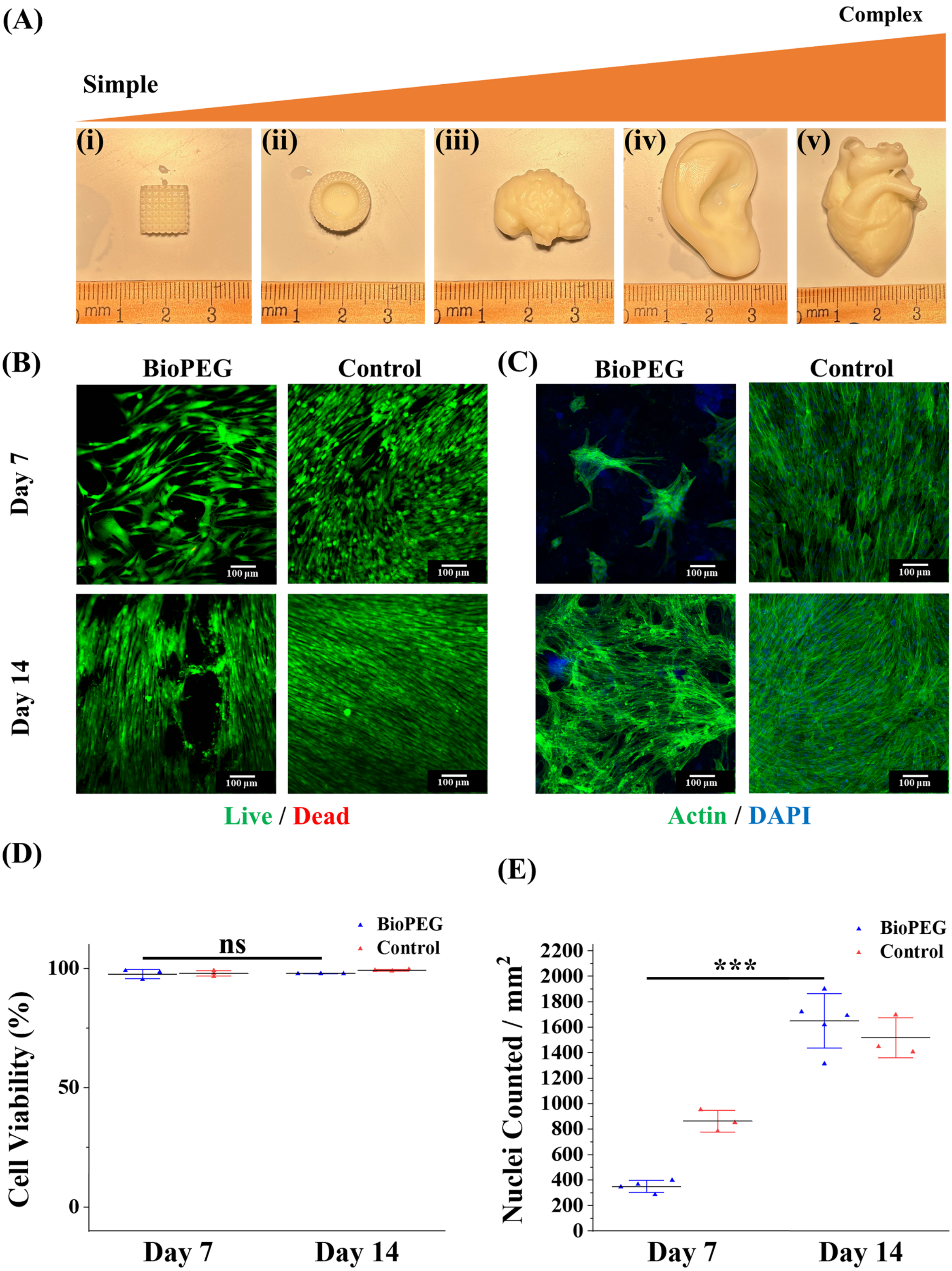

**Fig. 4. 3D bioprintability of the BioPEG hydrogel as a bio-ink.** (A) 3D printability of the BioPEG bio-ink in a variety of increasingly complex structures using Cellink Lumen-X Gen 1 light-based 3D printer. Structures printed were (i) simple lattice, (ii) porous cell culture well, (iii) brain, (iv) ear, and (v) veinous heart. Print settings used were 50 µm layer height, 50 % power (15.66 mW/cm$^2$), 6.25 s layer time, and 1X burn-in. **(B, C)** Fluorescence imaging of human mesenchymal stem cells (hMSCs) cultured on 3D printed BioPEG hydrogels for 7 and 14 days, showing good cytocompatibility. (B) Live and dead cells were stained with calcein-AM (green) and ethidium homodimer-1 (red), respectively. (C) Phalloidin conjugated with Alexa Fluor 488 fluorescent dye was used to stain cytoskeletal F-actin (green) and 4′,6-diamidino-2-phenylindole (DAPI) was used to stain cell nuclei (blue) **(scale bar: 100 µm).** Quantitative assessment included (D) cell viability derived from live and dead cell assay images, and (E) cell proliferation assessed through DAPI-stained cell nuclei counts on days 7 and 14 after cell seeding. Data represent means ± SD and statistical significance were determined by Student's *t*-test ($n = 3$ in (D), $n = 4$ or 5 for the BioPEG group and $n = 3$ for the control group in (E), $^*p < 0.05$, $^{**}p < 0.01$, $^{***}p < 0.001$, ns – non-significant).

Autodesk Fusion 360 software. A minimum of 4 samples were used for each test. Details of the BioPEG bio-ink preparation and sample printing process are mentioned in the subsections 4.16. *Formulation of BioPEG bio-ink* and 4.18. *DLP 3D printing using BioPEG bio-ink* below.

### 4.3. Mechanical characterization of BioPEG hydrogels

Mechanical assessment of the BioPEG hydrogels was conducted using an Instron 5969 dual-column testing system. Cuboid-shaped samples were fabricated via DLP 3D printing for subsequent compression analysis. Prior to testing, the samples were immersed in 1X PBS at 37 °C for 2 h. Compression testing was performed by subjecting the samples to a compression rate of 1 mm/min between two compression platens, recording the compression (mm) and compressive load (N) throughout each trial. The compression (mm) and compressive load (N) values were divided by the sample height and cross-sectional area to obtain the compressive strain and compressive stress (N/mm$^2$ or MPa), respectively. The slope of the compressive stress-strain curves in the linear region was calculated to determine the compressive modulus of the BioPEG hydrogel.

### 4.4. Degradation studies on BioPEG hydrogels

Degradation profiling of the BioPEG hydrogels was conducted following established protocols [25,26]. After lyophilization and weighing, the test samples were incubated in approximately 2 mL of 1X PBS within well plates, and housed in a cell culture incubator for a duration of 4 weeks. To ensure consistent activity, the buffer solutions were refreshed biweekly. At predefined intervals (1, 2, 3, and 4 weeks), 1X PBS solutions were aspirated, and the samples were subsequently lyophilized for 24 h before reweighing. The percentage of degradation (D%) was determined based on weight loss using Eq. (1).

$$D\% = \frac{Initial\ Dry\ Weight\ -\ Dry\ Weight\ at\ time\ t}{Initial\ Dry\ Weight} \times 100 \tag{1}$$

### 4.5. Swelling studies on BioPEG hydrogels

The equilibrium swelling ratio of 3D printed BioPEG hydrogels was assessed by preparing cuboid-shaped hydrogel samples via DLP 3D printing. After washing three times with 1X PBS, the samples were lyophilized and weighed under dry conditions. Subsequently, the samples were immersed in 1X PBS at 37 °C for 0, 2, 4, 6, 8, 12, 24, and 48 h, followed by reweighing after each immersion period. The swelling ratio is calculated as the ratio of the wet weight of the sample at each time point to the initial dry weight of the sample.

### 4.6. Preparation of TMSPMA-coated glass slides

Glass slides were prepared for 3-(trimethoxysilyl)propyl methacrylate (TMSPMA, Sigma-Aldrich) coating through an overnight treatment with 10 % (w/v) NaOH, followed by washing with 100 % (v/v) reagent alcohol comprising 90 % (v/v) ethanol, 5 % (v/v) methanol, and 5 % (v/v) isopropanol. The slides were baked at 80 °C for 1 hour and evenly coated with TMSPMA. Coated glass slides underwent overnight baking at 80 °C, followed by washing with 100 % (v/v) reagent alcohol, air-drying, and additional baking for 1–2 h at 80 °C. These coated glass slides were then cut into 1 cm x 1 cm pieces and stored in aluminum foil-wrapped containers until further use.

### 4.7. Preparation of PEGDA and BioPEG hydrogel discs for cell culture

PEGDA or BioPEG hydrogel solutions were deposited into a spacer and covered with TMSPMA-coated glass slide pieces, followed by photopolymerization using the Allevi 2 405 nm visible light to produce hydrogel discs of uniform dimensions (3 mm diameter, 0.4 mm height). A minimum of 4 samples were prepared per assay per time point per group.

### 4.8. Culture and maintenance of C2C12 cells and hMSCs

The immortalized mouse myoblast C2C12 cells and the hMSCs were purchased from Cell Applications Inc. For C2C12 cells, 15 % (v/v) fetal bovine serum (FBS, Gibco)-supplemented Dulbecco's Modified Eagle Medium (DMEM, Gibco) containing 1 % (v/v) Penicillin-Streptomycin (P/S, Gibco) was used. The hMSCs growth medium was composed of DMEM/F-12 medium supplemented with 15 % (v/v) FBS and 1 % (v/v) P/S. The C2C12 cells were passaged around 60–70 % confluency while the hMSCs were passaged around 70–80 % confluency. The freezing medium for either cell type was composed of the respective supplemented complete medium, FBS, and DMSO in the ratio of 5:4:1, respectively. Cells between passages 4 and 6 were used for all experiments.

### 4.9. Cell culture on the PEGDA and BioPEG hydrogels

Testing of PEGDA or BioPEG compatibility with C2C12 cells and hMSCs was performed according to our published protocols [25,26]. Briefly, 50,000 cells (C2C12 or hMSCs) were seeded onto the surface of PEGDA or BioPEG hydrogels in 24-well plates with 1 mL of the cell-specific growth medium. The cultures were maintained for 14 days, with assay time points on days 1, 7, and 14, at 37 °C in a 5 % $CO_2$ humidified incubator, with medium changes every 48 h. Cultures for differentiation experiments on BioPEG hydrogels were maintained for a total of 21 days, with assay time points on days 14 and 21. The cell experiments were repeated at least 3 times per cell type.

### 4.10. Myogenic differentiation of C2C12 cells on the BioPEG hydrogels

For the myogenic differentiation of C2C12 cells (between passages 4 and 6) on the BioPEG hydrogels, 50,000 C2C12 cells were seeded on the hydrogels, followed by pre-culture in the growth medium for 5 days. For induction of myogenic differentiation, low-serum DMEM consisting of 2 % (v/v) horse serum (Gibco), and 1 % P/S was utilized. The differentiation medium was refreshed every 2 days and samples were analyzed for myogenic differentiation on days 14 and 21.

### 4.11. Osteogenic differentiation of hMSCs on the BioPEG hydrogels

The osteogenic differentiation of hMSCs (between passages 4 and 6) on the BioPEG hydrogels was carried out based on a published protocol [43]. Briefly, 50,000 hMSCs were seeded atop the hydrogels, followed by pre-culture in the growth medium supplemented with 100 ng/mL basic fibroblast growth factor (bFGF, Reprocell) for 5 days. The medium was then changed to osteogenic differentiation induction medium, composed of low-glucose (1 g/L) DMEM (Gibco) supplemented with 10 % (v/v) FBS, 50 μg/mL l-ascorbic acid (Sigma-Aldrich), 10 mM β-glycerophosphate (Sigma-Aldrich), 100 nM dexamethasone (Sigma-Aldrich), and 1 % (v/v) P/S. The differentiation medium was refreshed every 2 days and samples were analyzed for osteogenic differentiation on days 14 and 21.

### 4.12. Cytocompatibility studies - cell viability, proliferation, and metabolic activity comparison on PEGDA and BioPEG hydrogels

The viability of C2C12 cells or hMSCs cultured on the hydrogels was assessed using a live/dead cell viability kit based on calcein-AM/ethidium homodimer-1, sourced from Invitrogen, adhering to the manufacturer's instructions. Cells were treated with a solution comprising 2 μM of calcein-AM and 4 μM of ethidium homodimer-1 in 1X Dulbecco's phosphate-buffered saline (DPBS) for 30–45 min at room temperature on days 1, 7, and 14 post-seeding. Fluorescent microscopic imaging was conducted utilizing a Zeiss LSM 880 inverted confocal microscope, where live cells emitted green fluorescence, and dead cells emitted red fluorescence. The utilization of ImageJ software facilitated the quantification of live cells relative to the total cell count, thereby evaluating cell viability.

For visualizing cellular cytoskeletal spreading and nuclear proliferation atop the hydrogel surfaces, fluorescent labeling of cytoskeletal actin filaments was accomplished using phalloidin conjugated with AlexaFluor 488, alongside DAPI (Biotium) staining of cell nuclei. Monolayer cultures were fixed at days 1, 7, and 14 post-cell seeding in 4 % (v/v) paraformaldehyde (ThermoFisher) for 15 min, followed by permeabilization in 0.1 % (v/v) Triton X-100 (Sigma Aldrich) for 20 min and blocking in 1 % (w/v) bovine serum albumin (BSA, Merck) for 45 min. Subsequent to fixation and permeabilization, the samples underwent three 1X PBS washes, each lasting 5 min. Application of AlexaFluor 488-labeled phalloidin (1/100 dilution in 0.1 % (w/v) BSA) to the samples ensued for 45 min, followed by three additional 1X PBS washes. Counterstaining with 1 μL/mL DAPI in 1X PBS for 5 min was performed, followed by a single 1X PBS wash prior to storage in 1X PBS for subsequent microscopic imaging. Fluorescent microscopic images were captured using a Zeiss LSM 880 inverted confocal microscope, with cellular proliferation quantified by enumerating DAPI-stained nuclei through the utilization of ImageJ software.

For the assessment of cellular metabolism in C2C12 cells or hMSCs, the PrestoBlue cell viability reagent (Invitrogen) was employed following the manufacturer's recommendations. Cells were exposed to culture medium supplemented with 10 % (v/v) PrestoBlue reagent for 3 h at 37 °C on days 1, 7, and 14 post-seeding. Subsequently, fluorescence intensity was measured using a Tecan fluorescence plate reader, with excitation at 560 nm and emission at 610 nm. Background fluorescence was established using blank wells devoid of cells, ensuring precise quantification of metabolic activity across all measurements.

### 4.13. Immunostaining for myogenic differentiation markers

To evaluate the expression of myogenic differentiation markers, specifically myogenin and myosin heavy chain-I (MHC-I), immunofluorescent staining was performed on monolayer cultures of differentiated C2C12 cells growing on BioPEG hydrogels. Fixation of cells with 4 % (v/v) paraformaldehyde for 15 min at room temperature was conducted on days 14 and 21 post-induction of myogenic differentiation of C2C12 cells on BioPEG hydrogels. Subsequently, samples underwent 1X PBS washing, permeabilization with 0.3 % (v/v) Triton X-100 for 15 min, and blocking with 1 % (v/v) BSA in 1X PBS containing 0.1 % (v/v) Triton X-100 for 1 hour. Following blocking, samples were incubated overnight with primary antibodies against myogenin (Abcam, ab124800, 1:500 dilution) and MHC-I (MF 20, DSHB, 1:500 dilution) in the blocking buffer at 4 °C. After three 1X PBS washes, myogenin samples were incubated with an Alexa Fluor 594-conjugated goat anti-mouse IgG ($H + L$) highly cross-adsorbed secondary antibody (Invitrogen, A-11032, 1:500 dilution), while MHC-I samples were incubated with an Alexa Fluor 488-conjugated goat anti-rabbit IgG ($H + L$) highly cross-adsorbed secondary antibody (Invitrogen, A-11034, 1:500 dilution), in the blocking buffer for 1 hour at room temperature. After three 1X PBS washes, samples were counterstained with 1 μL/mL DAPI in 1X PBS for 5 min at room temperature. Fluorescent microscopic imaging was conducted using a Zeiss LSM 880 inverted confocal microscope.

### 4.14. Immunostaining for osteogenic differentiation markers

To evaluate the expression of osteogenic differentiation markers, namely osteopontin (OPN) and osteocalcin (OCN), immunofluorescent staining of monolayer cultures of differentiated hMSCs growing on BioPEG hydrogels was conducted. Upon fixation of cells with 4 % (v/v) paraformaldehyde for 15 min at room temperature on days 14 and 21 post-initiation of osteogenic differentiation of hMSCs on BioPEG hydrogels, samples underwent 1X PBS washing, permeabilization with 0.3 % (v/v) Triton X-100 for 15 min, and blocking with 1 % (v/v) BSA in 1X PBS containing 0.1 % (v/v) Triton X-100 for 1 hour. Subsequently, samples were incubated overnight with primary antibodies against OPN (Proteintech, 22952–1-AP, 1:200 dilution) and OCN (Proteintech, 23418–1-AP, 1:200 dilution) in the blocking buffer at 4 °C. After three 1X PBS washes, samples were incubated with an Alexa Fluor 488-conjugated goat anti-rabbit IgG ($H + L$) highly cross-adsorbed secondary antibody (Invitrogen, A-11034, 1:500 dilution) in the blocking buffer for 1 hour at room temperature. After three 1X PBS washes, samples were counterstained with 1 μL/mL DAPI in 1X PBS for 5 min at room temperature. Fluorescent microscopic imaging was performed utilizing a Zeiss LSM 880 inverted confocal microscope.

### 4.15. Computational simulations studies

To determine the mechanism of the BIL adhesion to the cell membrane at the molecular level full atomistic MD simulations were applied. Because there is a lack of existing experimental data regarding the characteristics of the synthesized BIL, which could be used for comparison with the molecular attributes calculated through MD simulation techniques in the initial phase, the choice was made to utilize PEGDA as a reference polymer to verify the accuracy of the employed force fields in replicating the properties of the polymers. At the first step of the MD simulation, to check the force fields' ability to reproduce the PEGDA's properties, 100 chains of the polymer composing 20 monomers were randomly inserted in a cubic box ($10\times10\times10$ nm$^3$) (**Fig. S3**). After the energy minimization step (100,000), the temperature of the system was increased using an NVT ensemble from 0 to 300 K during 1000 ps with 1 fs time step. Then the structure of the PEGDA was equilibrated using NPT MD simulations including 50 ns (300 K), 10 ns (350 K), and 10 ns (300 K) with a 1 fs time step at 1 bar. Finally, 150 ns (2 fs time step) NPT MD (300 K and 1 bar) simulations were performed on the equilibrated structure as the product step. The calculated density value (1.12 g.cm$^{-3}$) for the corresponding polymer is in good agreement with the experimental value (1.16 g.cm$^{-3}$), confirming that the employed force field and MD protocols can reproduce the PEGDA properties (**Fig. S3**).

As can be seen from the Fig. 2**A** each branch of the cation part has three $NMe_3^+$ groups, therefore, each cation of the BIL has 9 positive charges. In the next step, to have a model of the BIL polymer to analyze its interactions with the membrane surface, multistep MD simulations were performed. Twenty-five cations along with 225 anions were added in a cubic box ($12 \times 12 \times 12$ nm$^3$) and 100,000 steps of energy minimization were performed to reduce the unfavorable contacts and to obtain a relaxed structure (**Fig. S4**). In the heating step, the temperature of the systems increased from 0 to 300 K during 10 ns (1 fs time step) in an NVT ensemble. Then the obtained structures were equilibrated during 70 ns (including 50 ns (300 K), 10 ns (350 K), and 10 ns (300 K)) with 1 fs time step in an NPT ensemble (1 bar). Finally, 150 ns NPT MD simulations were performed with a 2 fs time step on the obtained structure from the equilibration step. The obtained density for the BIL after the simulation time is $0.98 \pm 0.01$ g.cm$^{-3}$. In the next step, to have a structure of the solvated BIL in water the obtained structure of the BIL after 150 ns was immersed in a cubic box of water ($15\times15\times15$ nm$^3$). After minimization, heating, and equilibration steps, 100 ns NPT MD simulations (time step 2 fs) were performed to achieve a solvated model of the BIL (**Fig. S4**). This structure was used to analyze its interactions with the lipid membrane. In the next step of the simulations to elucidate the role of the BIL polymer on the properties of the lipid membrane (as a model of the cell membrane) the dynamical behavior of the DPPC lipid bilayer was investigated in the presence and absence of the BIL. The CHARMM-GUI server was used to model the initial structures of the lipid membranes [44]. The membranes were constructed from a fully hydrated bilayer composed of 300 DPPC units (**Fig. S5**). To analyze the role of cholesterol in the interactions between BIL and DPPC lipid membrane another lipid membrane was modeled including 90 monomers (7:3 ratio) of the cholesterol [20]. All the membranes (with/without cholesterol) were relaxed during 100,000 steps. Then 10 and 50 ns NVT and NPT MD simulations with 1 fs time step were performed as heating and equilibration steps, respectively. The typical force constant of 2.5 $kcal.mol^{-1}$. $Å^{-2}$ was applied for all the solute structures during the NVT simulations. Finally, 500 ns MD simulations (2 fs time step) were applied as the product step. In the next step, since the BIL behaves as a cell bio-adhesive, a double layer of the lipid membranes (with/without cholesterol) was designed to analyze BIL interactions with the lipid membranes (**Fig. S6**). The obtained structure of the mono-layer lipid membranes after 500 ns MD simulations was employed to design the double-layer membranes. The minimization, heating, and equilibration steps for the double lipid membrane are the same as conditions reported for the mono-layer membranes.

Water molecules were modeled using the TIP3P solvent model [45]. To neutralize the charge of the lipid membranes, antimicrobial peptides $Na^+$ and $Cl^-$ counter ions were added and all the simulations were performed at the physiological solution (150 mM NaCl). The LIPID17 [46] and General Amber Force Field (GAFF) parameters [47] were applied for the lipid membranes and BIL respectively. The atomic charges of the BIL were calculated by the CHelpG method at the M06–2X/6–31+*G*(d) level of theory using the Gaussian 16 computational software package [48, 49]. The periodic boundary conditions were applied in all directions for the studied systems. For the systems in the presence and absence of the lipid membranes, the anisotropic and isotropic Berendsen methods have been applied to control the pressure with a 1 ps relaxation time, respectively [50]. To regulate the temperature of the systems Langevin thermostat with 1 $ps^{-1}$ collision frequency was used [51]. To calculate the long-range electrostatic interactions using the Particle Mesh Ewald (PME) method, a 12 Å direct cut-off was applied [52]. The SHAKE constraints were used for all bonds involving hydrogen atoms [53]. All the above MD simulations were performed using the Amber 22 software package [54].

### 4.16. Formulation of BioPEG bio-ink

BioPEG bio-ink was prepared by mixing the following four components in 1X PBS: PEGDA, LAP, tartrazine, and BIL synthesized as per the aforementioned procedure. First, 0.2 % (w/v) LAP was added to 1X PBS in a covered vial and vortexed for 3 min until complete dissolution. Subsequently, tartrazine at 0.02 % (w/v) concentration (0.0001 g/μL) was added to the LAP solution. Following this, 15 % (w/v) BIL was incorporated, and vigorous vortexing ensued until homogeneity was attained. Sequentially, PEGDA was incrementally added by weight, with continuous vortexing until the solution achieved clarity without visible separation. pH adjustment to a cell-compatible pH of 7 was facilitated using 10 M NaOH, with verification of the final pH utilizing pH strips.

### 4.17. CAD model preparation and design

For the bio-ink testing phase, a total of seven CAD models were either adapted from existing designs or created anew. Utilizing Autodesk Fusion 360 2023 in conjunction with the Autodesk Lattice generation mesh package facilitated this process. The initial model comprised a simple card testing structure, designed in CAD. Subsequently, a 2 cm radius disk was designed specifically for cell culture seeding. The third model adopted a basic square lattice configuration, while the fourth model featured a cell culture well designed with a gyroid pattern. The remaining models were chosen to resemble anatomical features of the human body, including the ear, the brain, and the heart. These models were developed by modifying existing geometries, adjusting the base of the model, and scaling down dimensions accordingly. For easy access, the CAD models for the card, ear, brain, and heart structures are provided via the following links: Card:[https://www.thingiverse.com/thing:1019228], Ear: [https://www.thingiverse.com/thing:105808], Brain: [https://www.thingiverse.com/thing:169184], Heart: [https://www.thingiverse.com/thing:3173890].

### 4.18. DLP 3D printing using BioPEG bio-ink

The Lumen-X Gen 1 DLP bioprinter from Cellink facilitated the 3D printed scaffold fabrication. Optimized printing parameters included a layer height of 50 μm, power set at 50 % (15.66 $mW/cm^2$), layer exposure time of 6.25 s, and a burn-in factor of 1X. Polydimethylsiloxane (PDMS) plates from Cellink, in conjunction with the micro-etched glass print head, were utilized. Before printing, bio-ink was allowed to stabilize at room temperature for a minimum of one day and vigorously vortexed. Post-printing, scaffolds were rinsed with DI water while attached to the print head to eliminate residual uncured ink. Scaffolds were then carefully detached from the print head using a razor blade with a slow sawing motion. Subsequent immersion of scaffolds in a 250 mL water bath for 3–4 days facilitated tartrazine leaching, with continuous stirring and bi-daily water changes. Successful leaching was confirmed by inspecting samples and the leaching water for the absence of yellow tartrazine. For scaffold preparation before cell seeding, scaffolds were initially stored in 70 % (v/v) ethanol and exposed to UV light for 2 days. Following this, scaffolds underwent 1X PBS washes and 2 additional days of leaching to completely remove any residues. Daily 1X PBS exchanges were performed to optimize leaching efficiency.

### 4.19. Statistical analysis

At least 3 biological replicates were utilized for all the experiments. The datasets underwent statistical analysis utilizing IBM SPSS Statistics software (version 28), employing Student's *t*-test and one-way ANOVA test as applicable. Error bars were depicted as the mean ± standard deviation (SD) or standard error of the mean (SEM) of measurements. Levels of statistical significance were indicated as follows: ns - non-significant, $^*p < 0.05$, $^{**}p < 0.01$, $^{***}p < 0.001$.

## CRediT authorship contribution statement

**Aihik Banerjee:** Writing – review & editing, Writing – original draft, Visualization, Validation, Software, Methodology, Investigation, Formal analysis, Data curation, Funding acquisition. **Mohammad Khavani:** Writing – review & editing, Writing – original draft, Visualization, Validation, Software, Methodology, Investigation, Formal analysis, Data curation. **Kevin Dalsania:** Writing – review & editing, Writing – original draft, Validation, Software, Methodology, Investigation, Formal analysis, Data curation, Visualization. **Prince David Okoro:** Visualization, Formal analysis, Data curation, Investigation. **Mohammad R.K. Mofrad:** Conceptualization, Funding acquisition, Methodology, Project administration, Resources, Supervision, Writing – review & editing. **Iman Noshadi:** Writing – review & editing, Supervision, Resources, Project administration, Methodology, Funding acquisition, Conceptualization.

## Declaration of competing interest

The authors declare the following financial interests/personal relationships which may be considered as potential competing interests:

Iman Noshadi reports financial support was provided by University of California Riverside. Iman Noshadi reports financial support was provided by National Science Foundation. Aihik Banerjee reports financial support was provided by California Institute for Regenerative Medicine. If there are other authors, they declare that they have no known competing financial interests or personal relationships that could have appeared to influence the work reported in this paper.

## Data availability

Data will be made available on request.

## Acknowledgements

The authors are grateful for financial support from the UC Riverside Startup Fund, NSF 1919092, 2136603, and 2232153 awards, and the CIRM-TRANSCEND Training Grant (Award #: EDUC4-12752).

## Supplementary materials

Supplementary material associated with this article can be found, in the online version, at doi:10.1016/j.apmt.2024.102444.

## References

[1] E.J. Lee, F.K. Kasper, A.G. Mikos, Biomaterials for tissue engineering, Ann. Biomed. Eng 42 (2013) 323–337, https://doi.org/10.1007/s10439-013-0859-6.

[2] A.E. Eldeeb, S. Salah, N.A. Elkasabgy, Biomaterials for tissue engineering applications and current updates in the field: a comprehensive review, AAPS PharmSciTech 23 (2022), https://doi.org/10.1208/s12249-022-02419-1.

[3] M. Brovold, J.I. Almeida, I. Pla-Palacín, P. Sainz-Arnal, N. Sánchez-Romero, J. J. Rivas, et al., Naturally-derived biomaterials for tissue engineering applications, Adv. Exp. Med. Biol. (2018) 421–449, https://doi.org/10.1007/978-981-13-0947-2_23.

[4] Z. Terzopoulou, A. Zamboulis, I. Koumentakou, G. Michailidou, M.J. Noordam, D. N. Bikiaris, Biocompatible synthetic polymers for tissue engineering purposes, Biomacromolecules 23 (2022) 1841–1863, https://doi.org/10.1021/acs.biomac.2c00047.

[5] S. Liu, J.-M. Yu, Y.-C. Gan, X.-Z. Qiu, Z.-C. Gao, H. Wang, et al., Biomimetic natural biomaterials for tissue engineering and regenerative medicine: new biosynthesis methods, recent advances, and emerging applications, Mil. Med. Res 10 (2023), https://doi.org/10.1186/s40779-023-00448-w.

[6] A.S. Tripathi, M.E. Zaki, S.A. Al-Hussain, B.K. Dubey, P. Singh, L. Rind, et al., Material matters: exploring the interplay between natural biomaterials and host immune system, Front. Immunol 14 (2023), https://doi.org/10.3389/fimmu.2023.1269960.

[7] D. Salthouse, K. Novakovic, C.M.U. Hilkens, A.M. Ferreira, Interplay between biomaterials and the immune system: challenges and opportunities in regenerative medicine, Acta Biomater 155 (2023) 1–18, https://doi.org/10.1016/j.actbio.2022.11.003.

[8] A. Kamatar, G. Gunay, H. Acar, Natural and synthetic biomaterials for engineering multicellular tumor spheroids, Polymers (Basel) 12 (2020) 2506, https://doi.org/10.3390/polym12112506.

[9] A. Khalili, M. Ahmad, A review of cell adhesion studies for Biomedical and biological applications, Int. J. Mol. Sci 16 (2015) 18149–18184, https://doi.org/10.3390/ijms160818149.

[10] F. Karimi, A.J. O'Connor, G.G. Qiao, D.E. Heath, Integrin clustering matters: a review of biomaterials functionalized with multivalent integrin-binding ligands to improve cell adhesion, migration, differentiation, angiogenesis, and biomedical device integration, Adv. Healthc. Mater 7 (2018), https://doi.org/10.1002/adhm.201701324.

[11] V.B. Kumar, O.S. Tiwari, G. Finkelstein-Zuta, S. Rencus-Lazar, E. Gazit, Design of functional RGD peptide-based biomaterials for tissue engineering, Pharmaceutics 15 (2023) 345, https://doi.org/10.3390/pharmaceutics15020345.

[12] M. Yang, Z.-C. Zhang, Y. Liu, Y.-R. Chen, R.-H. Deng, Z.-N. Zhang, et al., Function and mechanism of RGD in bone and cartilage tissue engineering, Front. Bioeng. Biotechnol 9 (2021), https://doi.org/10.3389/fbioe.2021.773636.

[13] M. Tallawi, E. Rosellini, N. Barbani, M.G. Cascone, R. Rai, G. Saint-Pierre, et al., Strategies for the chemical and biological functionalization of scaffolds for Cardiac Tissue Engineering: a Review, J. Royal Soc. Interface 12 (2015) 20150254, https://doi.org/10.1098/rsif.2015.0254.

[14] X. Wang, H. Wang, K. Jiang, Y. Zhang, C. Zhan, M. Ying, et al., Liposomes with cyclic RGD peptide motif triggers acute immune response in mice, J. Control. Release 293 (2019) 201–214, https://doi.org/10.1016/j.jconrel.2018.12.003.

[15] E. Mariani, G. Lisignoli, R.M. Borzì, L. Pulsatelli, Biomaterials: foreign bodies or tuners for the immune response? Int. J. Mol. Sci 20 (2019) 636, https://doi.org/10.3390/ijms20030636.

[16] R.A. Pérez, J.-E. Won, J.C. Knowles, H.-W. Kim, Naturally and synthetic smart composite biomaterials for tissue regeneration, Adv. Drug Deliv. Rev. 65 (2013) 471–496, https://doi.org/10.1016/j.addr.2012.03.009.

[17] M.S. Reddy, D. Ponnamma, R. Choudhary, K.K. Sadasivuni, A comparative review of natural and synthetic biopolymer composite scaffolds, Polymers 13 (2021) 1105, https://doi.org/10.3390/polym13071105.

[18] Q. Li, C. Wen, J. Yang, X. Zhou, Y. Zhu, J. Zheng, et al., Zwitterionic biomaterials, Chem. Rev. 122 (2022) 17073–17154, https://doi.org/10.1021/acs.chemrev.2c00344.

[19] X. Chen, H. Shang, S. Cao, H. Tan, J. Li, A zwitterionic surface with general cell-adhesive and protein-resistant properties, RSC Adv 5 (2015) 76216–76220, https://doi.org/10.1039/c5ra16883j.

[20] X. Yu, Z. Liu, J. Janzen, I. Chafeeva, S. Horte, W. Chen, et al., Polyvalent choline phosphate as a universal biomembrane adhesive, Nat. Mater 11 (2012) 468–476, https://doi.org/10.1038/nmat3272.

[21] K. Qu, Z. Yuan, Y. Wang, Z. Song, X. Gong, Y. Zhao, et al., Structures, properties, and applications of zwitterionic polymers, ChemPhysMater 1 (2022) 294–309, https://doi.org/10.1016/j.chphma.2022.04.003.

[22] C.-P. Shih, X. Tang, C.W. Kuo, D.-Y. Chueh, P. Chen, Design principles of bioinspired interfaces for biomedical applications in therapeutics and imaging, Front. Chem 10 (2022), https://doi.org/10.3389/fchem.2022.990171.

[23] B. Kanjilal, Y. Zhu, V. Krishnadoss, J.M. Unagolla, P. Saemian, A. Caci, et al., Bioionic liquids: enabling a paradigm shift toward advanced and smart biomedical applications, Adv. Intell. Syst 5 (2023), https://doi.org/10.1002/aisy.202200306.

[24] J.M. Gomes, S.S. Silva, R.L. Reis, Biocompatible ionic liquids: fundamental behaviours and applications, Chem. Soc. Rev 48 (2019) 4317–4335, https://doi.org/10.1039/c9cs00016j.

[25] I. Noshadi, B.W. Walker, R. Portillo-Lara, E. Shirzaei Sani, N. Gomes, M. R. Aziziyan, et al., Engineering biodegradable and biocompatible bio-ionic liquid conjugated hydrogels with tunable conductivity and mechanical properties, Sci. Rep 7 (2017), https://doi.org/10.1038/s41598-017-04280-w.

[26] V. Krishnadoss, B. Kanjilal, A. Masoumi, A. Banerjee, I. Dehzangi, A. Pezhouman, et al., Programmable bio-ionic liquid functionalized hydrogels for in situ 3D bioprinting of electronics at the tissue interface, Mater. Today Adv 17 (2023) 100352, https://doi.org/10.1016/j.mtadv.2023.100352.

[27] Y. Wang, S. Zhang, J. Wang, Photo-crosslinkable hydrogel and its biological applications, Chin. Chem. Lett. 32 (2021) 1603–1614, https://doi.org/10.1016/j.cclet.2020.11.073.

[28] B. Yi, Q. Xu, W. Liu, An overview of substrate stiffness guided cellular response and its applications in tissue regeneration, Bioact. Mater. 15 (2022) 82–102, https://doi.org/10.1016/j.bioactmat.2021.12.005.

[29] M. Sun, G. Chi, J. Xu, Y. Tan, J. Xu, S. Lv, Z. Xu, Y. Xia, L. Li, Y. Li, Extracellular matrix stiffness controls osteogenic differentiation of mesenchymal stem cells mediated by integrin α5, Stem Cell. Res. Ther. 9 (2018) 52, https://doi.org/10.1186/s13287-018-0798-0.

[30] S. Cai, C. Wu, W. Yang, W. Liang, H. Yu, L. Liu, Recent advance in surface modification for regulating cell adhesion and behaviors, Nanotechnol. Rev. 9 (2020) 971–989, https://doi.org/10.1515/ntrev-2020-0076.

[31] M. Tallawi, E. Rosellini, N. Barbani, M.G. Cascone, R. Rai, G. Saint-Pierre, A. R. Boccaccini, Strategies for the chemical and biological functionalization of scaffolds for cardiac tissue engineering: a review, J. R. Soc. Interface. 12 (2015) 20150254, https://doi.org/10.1098/rsif.2015.0254.

[32] H.S. Kim, S.G. Kumbar, S.P. Nukavarapu, Biomaterial-directed cell behavior for tissue engineering, Curr. Opin. Biomed. Eng. 17 (2021) 100260, https://doi.org/10.1016/j.cobme.2020.100260.

[33] Y. Bagheri, A.A. Ali, M. You, Current methods for detecting cell membrane transient interactions, Front. Chem 8 (2020), https://doi.org/10.3389/fchem.2020.603259.

[34] Q. Zhang, S. Li, Y. Yang, Y. Shan, H. Wang, Studying structure and functions of cell membranes by single molecule biophysical techniques, Biophys. Reports 7 (2021) 384–398, https://doi.org/10.52601/bpr.2021.210018.

[35] A.R. Montes, G. Gutierrez, A. Buganza Tepole, M.R.K. Mofrad, Multiscale computational framework to investigate integrin mechanosensing and cell adhesion, J. Appl. Phys. 134 (2023) 114702, https://doi.org/10.1063/5.0164826.

[36] A. Shamloo, M. Sarmadi, Investigation of the adhesive characteristics of polymer–protein systems through molecular dynamics simulation and their relation to cell adhesion and proliferation, Integr. Biol. 8 (2016) 1276–1295, https://doi.org/10.1039/c6ib00159a.

[37] T.C. Bidone, D.J. Odde, Multiscale models of integrins and cellular adhesions, Curr. Opin. Struct. Biol. 80 (2023) 102576, https://doi.org/10.1016/j.sbi.2023.102576.

[38] G. Saini, N. Segaran, J. Mayer, A. Saini, H. Albadawi, R. Oklu, Applications of 3D bioprinting in tissue engineering and regenerative medicine, J. Clin. Med 10 (2021) 4966, https://doi.org/10.3390/jcm10214966.

[39] A. Sachdev, S. Acharya, T. Gadodia, S. Shukla, H. J, C. Akre, et al., A review on techniques and biomaterials used in 3D bioprinting, Cureus (2022), https://doi.org/10.7759/cureus.28463.

[40] H. Li, J. Dai, Z. Wang, H. Zheng, W. Li, M. Wang, et al., Digital light processing (DLP)-based (bio)printing strategies for tissue modeling and regeneration, aggregate. 4 (2022). doi:10.1002/agt2.270.

[41] K. Yu, X. Zhang, Y. Sun, Q. Gao, J. Fu, X. Cai, et al., Printability during projection-based 3D bioprinting, Bioactive Mater 11 (2022) 254–267, https://doi.org/10.1016/j.bioactmat.2021.09.021.

[42] J.R. dos Santos, L. de Sousa Soares, B.M. Soares, M. de Gomes Farias, V.A. de Oliveira, N.A. de Sousa, et al., Cytotoxic and mutagenic effects of the food additive tartrazine on Eukaryotic cells, BMC Pharmacol. Toxicol 23 (2022), https://doi.org/10.1186/s40360-022-00638-7.

[43] Y. Tai, S. Yang, S. Yu, A. Banerjee, N.V. Myung, J. Nam, Modulation of piezoelectric properties in electrospun PLLA nanofibers for application-specific self-powered stem cell culture platforms, Nano Energy 89 (2021) 106444, https://doi.org/10.1016/j.nanoen.2021.106444.

[44] E.L. Wu, X. Cheng, S. Jo, H. Rui, K.C. Song, E.M. Dávila-Contreras, et al., CHARMM-Gui *membrane builder* toward realistic biological membrane simulations, J. Comput. Chem 35 (2014) 1997–2004, https://doi.org/10.1002/jcc.23702.

[45] W.L. Jorgensen, J. Chandrasekhar, J.D. Madura, R.W. Impey, M.L. Klein, Comparison of simple potential functions for simulating liquid water, J. Chem. Phys. 79 (1983) 926–935, https://doi.org/10.1063/1.445869.

[46] Å.A. Skjevik, B.D. Madej, C.J. Dickson, C. Lin, K. Teigen, R.C. Walker, et al., Simulation of lipid bilayer self-assembly using all-atom lipid force fields, Phys. Chem. Chem. Phys 18 (2016) 10573–10584, https://doi.org/10.1039/c5cp07379k.

[47] J. Wang, R.M. Wolf, J.W. Caldwell, P.A. Kollman, D.A. Case, Development and testing of a general amber force field, J. Comput. Chem 25 (2004) 1157–1174, https://doi.org/10.1002/jcc.20035.

[48] Y. Zhao, D.G. Truhlar, A new local density functional for main-group thermochemistry, transition metal bonding, thermochemical kinetics, and noncovalent interactions, J. Chem. Phys. 125 (2006), https://doi.org/10.1063/1.2370993.

[49] M.E. Frisch, G.W. Trucks, H.B. Schlegel, G.E. Scuseria, M.A. Robb, J.R. Cheeseman, et al., Gaussian 16, Revision C. 01, Gaussian Inc., Wallingford, CT, 2016.

[50] B.P. Uberuaga, M. Anghel, A.F. Voter, Synchronization of trajectories in canonical molecular-dynamics simulations: observation, explanation, and exploitation, J. Chem. Phys. 120 (2004) 6363–6374, https://doi.org/10.1063/1.1667473.

[51] D.J. Sindhikara, S. Kim, A.F. Voter, A.E. Roitberg, Bad seeds sprout perilous dynamics: stochastic thermostat induced trajectory synchronization in biomolecules, J. Chem. Theor. Comput 5 (2009) 1624–1631, https://doi.org/10.1021/ct800573m.

[52] T. Darden, D. York, L. Pedersen, Particle mesh ewald: an $n \cdot \log(n)$ method for Ewald sums in large systems, J. Chem. Phys. 98 (1993) 10089–10092, https://doi.org/10.1063/1.464397.

[53] J.-P. Ryckaert, G. Ciccotti, H.J.C. Berendsen, Numerical integration of the Cartesian equations of motion of a system with constraints: molecular dynamics of N-Alkanes, J. Comput. Phys. 23 (1977) 327–341, https://doi.org/10.1016/0021-9991(77)90098-5.

[54] D.A. Case, H.M. Aktulga, K. Belfon, I. Ben-Shalom, S.R. Brozell, D.S. Cerutti, et al., Amber 2021, University of California, San Francisco, 2021.